Journal of Alloys and Compounds 735 (2018) 277–284

Contents lists available at ScienceDirect

Journal of Alloys and Compounds

journal homepage: http://www.elsevier.com/locate/jalcom

Experimental and theoretical study of hydrogen desorption process from $Mn(BH_4)_2$

Ilia A. Pankin [a, b], Alexander A. Guda [a, *], Nikolay A. Tumanov [c], Yaroslav Filinchuk [c], Kirill A. Lomachenko [a, d], Aram L. Bugaev [a, b], Sergey A. Guda [e], Victor V. Shapovalov [a], Carlo Lamberti [a, b, f], Alexander V. Soldatov [a]

[a] The Smart Materials Research Center, Southern Federal University, Sladkova 178/24, 344090, Rostov-on-Don, Russia
[b] Department of Chemistry, INSTM Reference Center and CrisDi Interdepartmental Center for Crystallography, University of Torino, via Giuria 7, I-10125, Torino, Italy
[c] Institute of Condensed Matter and Nanosciences, Universite Catholique de Louvain, Place L. Pasteur 1, 1348, Louvain-la-Neuve, Belgium
[d] European Synchrotron Radiation Facility, 71 avenue des Martyrs, 38043, Grenoble, France
[e] Institute of mathematics, mechanics and computer science, Southern Federal University, Milchakova 8a, 344090, Rostov-on-Don, Russia
[f] Department of Physics and NIS Interdepartmental Center, University of Torino, via Giuria 1, I-10125, Torino, Italy

ARTICLE INFO

Article history:
Received 27 June 2017
Received in revised form
29 October 2017
Accepted 5 November 2017
Available online 7 November 2017

Keywords:
Hydrogen desorption
Manganese borohydride
Amorphization
X-ray absorption spectroscopy
Structure predictions
Evolutionary algorithm

ABSTRACT

The thermal decomposition of manganese borohydride $Mn(BH_4)_2$ was studied by means of synchrotron-based X-ray absorption spectroscopy (XAS), X-ray powder diffraction (XRPD) and theoretical density functional (DFT) modeling aiming to elucidate changes of the local atomic structure upon hydrogen desorption and to determine possible decomposition reaction products. XRPD patterns indicate profound structural changes in the material above 120 °C with subsequent amorphization. DFT simulations predict the collapse of the highly porous framework structure upon hydrogen desorption and significant reduction of Mn-B and Mn-Mn interatomic distances by 19% and 41% respectively. These estimations are in a good agreement with the quantitative analysis of the X-ray absorption spectra above Mn K-edge. Based on XAS we derive possible decomposition products and reaction path. In particular, the amount of Mn metallic phase was estimated to be less than 5% after the heating up to 200 °C. Several structural models for the final state of manganese borohydride in a heating process are constructed by means of energy minimization in conjunction with evolutionary algorithms.

1. Introduction

Solid state hydrogen storage materials represent a perspective, compact and safe way to store hydrogen energy [1-5]. High gravimetric and volumetric density of hydrogen, the low temperature of desorption and cycling ability are the main requirements for the potential hydrogen-storage materials [6]. The most efficient hydrogen absorbers nowadays are alkali metal borohydrides. However, the high temperature of desorption (e.g. above 400 °C for $LiBH_4$ [7-13]) and a limited number of charge/discharge cycles makes their use unjustified. Many of borohydrides yield upon heating stable $[B_{12}H_{12}]^{2-}$ species that decrease their hydrogen release potential and prevent their reversibility. This behavior is one of the obstacles for $Mg(BH_4)_2$ rehydrogenation [6,14]. Another one is the amorphization process which accompanies hydrogen release from the porous structure [15].

Manganese borohydride α-$Mn(BH_4)_2$ is structurally similar to α-$Mg(BH_4)_2$ – a perspective material which is considered to be a high-capacity (theoretical hydrogen capacity of 9.53 wt.%) solid-state hydrogen storage candidate, but so far has not been shown to exhibit reversible hydrogenation. $Mn(BH_4)_2$, among all other transition complex borohydrides, is stable at room temperature [16]. It can be synthesized by ball-milling of a mixture of the alkali metal borohydride MBH_4 (M = Li, Na for instance) and anhydrous manganese chloride $MnCl_2$ [17]. Density functional theory (DFT) calculations suggested that *I*-4m2 structure is the most

* Corresponding author.
E-mail address: guda@sfedu.ru (A.A. Guda).

https://doi.org/10.1016/j.jallcom.2017.11.062
0925-8388/

energetically favorable for $Mn(BH_4)_2$ [16], however crystallographic characterization revealed a structure with a trigonal crystal system with a space group of $P3_112$ [17]. This structure was also obtained by solvent synthesis with a molar ratio 2:1 and 3:1 of lithium borohydride to manganese chloride [18,19]. A porous atomic structure of γ-$Mn(BH_4)_2$ isostructural to the magnesium analog [20] was also found recently, the large pores make them similar to metal-organic framework structures (MOFs) [19]. Porous channels are located along ***c*** crystallographic axis and have a size up to 6.5 Å at a cross section - thus the material is able to absorb gas molecules in addition to inner hydrogen atoms in the framework structure [20]. At high-pressure dense manganese borohydride phase is formed which is not stable at ambient conditions. It has a high volumetric and gravimetric hydrogen content and can be of interest for hydrogen storage as practically pure hydrogen is desorbed upon heating [21].

DFT is considered to be a versatile and important tool to solve research problems in metal-hydrogen interactions and establish associated mechanisms [6]. The thermodynamical stability, structural, electronic, dielectric, and vibrational properties for several metal borohydrides, $M(BH_4)_n$ (M = Li, Be, Na, Mg, Ca, K, Cu, Mg, Zn, Sc, Zr, Y, and Hf; n = 1–4) have been widely investigated [14,22-28]. Theoretical study of the most probable decomposition path of $Mn(BH_4)_2$ based on DFT calculations of the enthalpy of formation in conjunction with Gibbs energy [16] suggested the following possible decomposition reactions:

$$Mn(BH_4)_2 \rightarrow Mn + 2B + 4H_2 \quad (1.a)$$

$$Mn(BH_4)_2 \rightarrow MnH_2 + 2B + 3H_2 \quad (1.b)$$

$$Mn(BH_4)_2 \rightarrow MnB_2 + 4H_2 \quad (1.c)$$

$$Mn(BH_4)_2 \rightarrow MnH_2 + B_2H_6 \quad (1.d)$$

$$Mn(BH_4)_2 \rightarrow Mn + B_2H_6 + H_2 \quad (1.e)$$

A quantitative analysis of standard-state enthalpy of reaction and Gibbs energy calculations reveal that decomposition path (1.a) is the most feasible dehydrogenation reaction [16]. However the absence of Mn metallic reflections in the X-ray powder diffraction (XRPD) patterns obtained for different molar ratio $LiBH_4$-$MnCl_2$ mixture after heating can be explained by forming an amorphous Mn-B compound, such as amorphous manganese borides MnB, MnB_2 or Mn_3B_4 [29]. Several possible manganese boride stoichiometries in equation (1.c) were also revealed by thermal analysis [29]. However, Liu et al. [30] found that samples prepared by ball milling of the $LiBH_4 + MnCl_2$ after decomposition form amorphous boron and metallic manganese without any features in FTIR spectra corresponding to Mn-B vibrations.

Understanding of the decomposition mechanism is important for the practical use of $Mn(BH_4)_2$-based materials and development of reversible hydrogen sorption reaction pathways. Borohydrides of transition metals unlike borohydrides of alkali metals MBH_4 (containing light elements M = Li, Na etc.) allow measuring X-ray absorption spectra (XAS) without complicated vacuum conditions. Thus in-situ XRPD can be combined with the local probe of Mn K-edge XAS spectra. In our work, we address the problem of the $Mn(BH_4)_2$ decomposition using in-situ XRPD and XAS spectroscopy which probes long-range crystalline order and local atomic structure around Mn atoms, respectively. DFT simulations combined with evolutionary algorithms provided series of the structures for the Mn-B system after hydrogen decomposition which were subsequently verified with XAS data and allowed to determine thermal decomposition pathway for $Mn(BH_4)_2$.

2. Methods

2.1. Experimental details

The trigonal α-$Mn(BH_4)_2$ was obtained by wet chemical methods from $NaBH_4$ and $MnCl_2$ in ether solution according to the protocol described in Ref. [17]. XRPD analysis excludes NaCl phase or solvates and reveals a small amount of residual $NaBH_4$ (see Fig. S1 in SI).

In-situ XAS and XRPD measurements were performed at Swiss-Norwegian Beamline BM01B of the European Synchrotron Radiation Facility [31,32], now moved to the BM31 port. The sample powder was placed inside a glovebox into 1 mm glass capillary. The capillary was glued into a metal sample holder equipped with two one-way valves from the both sides and then transferred to a pressurized setup at the beamline which provided remote control of the gas content and pressure inside the capillary. The capillary was oriented horizontally and perpendicularly to the X-ray beam.

Under each condition, both XAS and XRPD measurements were performed. The beamline allows a rapid (about 30 s) plug and play switch between X-ray absorption and X-ray diffraction setups [33,34]. Mn K-edge XAS data were collected in fluorescence mode, using a 13 element silicon solid-state detector, in the energy range of 6.5–6.7 keV employing a double-crystal Si(111) monochromator in the continuous scanning mode. The energy was calibrated with a Mn foil. Self-absorption correction was made via Athena software package [35]. XRPD patterns were recorded by the CMOS (complementary metal-oxide-semiconductor) - Dexela 2D detector. Each pattern was recorded with an acquisition time of 15 s and was followed by a dark scan used for background subtraction. The λ and the sample to detector distance and tilts, were calibrated using Si and LaB_6 powder NIST (National Institute of Standards and Technology) standards and kept fixed in the refinements of the Mn-B-hydrate samples. For XRPD the wavelength of the incident radiation was refined to be 0.5132(3) Å. XRPD patterns were obtained before measuring each subsequent X-ray absorption spectrum. The resulting 2D images were integrated using Fit 2D software [36].

2.2. Computational details

To simulate Mn K-edge XAS spectra we used finite difference method [37] and full potential approximation implemented in the FDMNES software [38,39]. Sparse solvers for the finite difference matrix were used in order to decrease the required computational time [40,41].

Spin-polarized DFT simulations were performed using plane-wave pseudopotential approach implemented in the VASP 5.2 package [42-44]. Cell shape, cell volume, and atomic positions were used as variable parameters in the geometry relaxation procedure. Block Davidson scheme for SCF cycles calculations was used and conjugate gradients [45] methods of energy minimization were applied to study the collapse of the initial porous structure upon removing hydrogen atoms. A kinetic energy cutoff of 450 eV was used for the plane wave basis set. $3 \times 3 \times 3$ and $7 \times 7 \times 7$ K-point meshes automatically generated according to Monokhorts-Pack scheme [46] was implemented for sampling the Brillouin zone for large porous cell and for collapsed Mn-B system, respectively.

Structure prediction for Mn-B system was performed using USPEX code [47-49] based on an evolutionary algorithm. Ab-initio free energy obtained by VASP 5.2 calculations was employed as an evolutionary function. USPEX calculations were performed for the Mn:B system with stoichiometries 2:1, 1:1, 1:2, and 1:4 with a total number of atoms in the unit cell ranging from 20 to 30 atoms. More than 600 structural models for each of the unit cells were generated and verified according to their free energy. Each run of the

evolutionary algorithm started with the production of an initial population of 18–20 structures by the random way. At each step of the run, the structures were fully relaxed. We made local optimization in three subsequent steps for each structure increasing the precision of input parameters for VASP. The three best structures with the lowest free energy among current generation are survived for the next generation without any structural changes. The worst structures were discarded, the others were considered as "parent" structures for the next generation and treated by different types of variation operators. The probability for different variations to be applied was set up as 0.55, 0.2, 0.15, 0.1 for heredity, random, softmutation and permutation respectively thus the most frequently used variation operators were heredity and atomic position mutation. The convergence was achieved if the same structural model had the lowest energy for six subsequent generations.

3. Results and discussion

3.1. Amorphization process upon hydrogen release

Fig. 1 shows thermogravimetric analysis (TGA) of the sample powder (part a) and the in-situ XRPD patterns upon heating (part b). TGA reveal the drastic weight loss of the sample starting from 140 °C, while changes in XRPD patterns and XAS spectra (not reported for brevity) indicate phase transition occurring already at 120 °C. The observed mass loss in the temperature range from 120 °C to 160 °C corresponds to the desorption of all hydrogen atoms from the lattice. The presence of small amount of sodium borohydride can be revealed by smooth step in TGA starting from 250 °C and by XRD analysis shown in Figs. S1 and S2 (see SI).

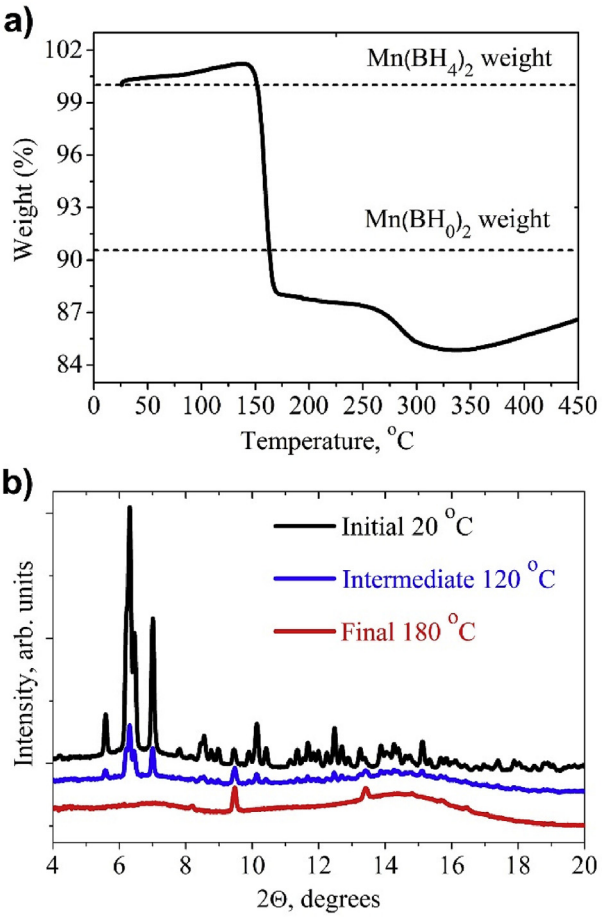

Fig. 1. (a) TGA analysis for the sample in the temperature range 0–450 °C (b) Selected XRPD patterns obtained in-situ during heating in vacuum.

The rapid decrease of the XRPD peaks intensities accompanied by the formation of broad maxima centered at ~7.0° and 14.5° clearly justify an amorphization of the initial material [50]. Combined with drastic weight loss, observed by TGA the amorphous phase can be related to Mn-B system. Similar behavior of powder diffraction data for pressure-dependent measurements was described for the related $Mg(BH_4)_2$ [20]: stable crystalline cubic γ-phase transforms into an amorphous material which then transforms into the dense tetragonal δ-phase. In the latter case, an amorphous borohydride of magnesium is the intermediate phase between two other stable crystalline γ-phase and high-pressure polymorph - δ-phase [20]. The pressure-collapsed amorphous phase of $Mg(BH_4)_2$ can be converted back to the porous framework structure after heating $Mg(BH_4)_2$ [6]. Recently Varin et al. [51] reported a new mechano-chemically synthesized amorphous manganese borohydride which is able to restore crystalline structure after solvent filtration and extraction even at low temperature. However, we didn't observe reversible porous structure formation in XRPD after the sample was cooled down back to room temperature both in an inert atmosphere and in hydrogen. This can be explained by the destruction of $[BH_4]^-$ units upon hydrogen desorption which support porous phase.

3.2. DFT modeling of the structure collapse upon hydrogen release

As a first approximation to the dehydration process, we have performed lattice relaxation for the initial $Mn(BH_4)_2$ porous structure [17] and hydrogen deficient structures where hydrogen atoms were randomly removed. In order to find the global minimum, both cell parameters and atomic positions were allowed to relax and conjugate gradient algorithm [45] was employed to optimize atomic positions for the structure without hydrogen. Fig. 2 shows the equilibrium volume for the unit cell with 100% occupancy ($Mn(BH_4)_2$ further referred as VASP#1) of hydrogen positions, 50% ($Mn(BH_2)_2$ further referred as VASP#2) and 0% occupancy ($Mn(BH_0)_2$ further referred as VASP#3).

Table 1 summarizes the calculated structural parameters for the fully hydrated and dehydrated structures compared to the experimental XRPD values for the initial structure. The mean values for interatomic distances reported in Table 1 were calculated by averaging over all nine non-equivalent Mn positions in the unit cell. The standard deviation for the nearest Mn-B and Mn-Mn distances are reported together with their mean values and provide an estimation of the disorder in the local coordination of Mn. Calculated structural parameters for the initial fully hydrated structure are in a good agreement with experimental data [17]. The difference between experimental and calculated Mn-B distances and unit cell volume is 1.2% and 2.2% correspondingly. A significant decrease of the average Mn-Mn distance by 43% (from 4.77 Å to 2.72 Å) after dehydrogenation is explained by the degradation of the porous structure upon removal of hydrogen atoms. This process is accompanied by cell volume reduction from 998.8 $Å^3$ to 216.9 $Å^3$. Average Mn-B distance in collapsed $Mn(BH_0)_2$ structure is contracted by 10% (from 2.41 Å to 2.17 Å) and is comparable with results obtained by Severa et., al. [52] for the Mn-B distance in isolated $[Mn(BH_4)_4]^{2-}$ clusters.

Results of the DFT simulations are further supported by means of X-ray absorption spectroscopy analysis. This method is sensitive to the local atomic structure and electronic configuration of absorbing atoms [53-56]. It is thus, in general, an appropriate technique to study materials without long-range atomic order [57-59] and amorphous phase of dehydrated $Mn(BH_4)_2$ in the present

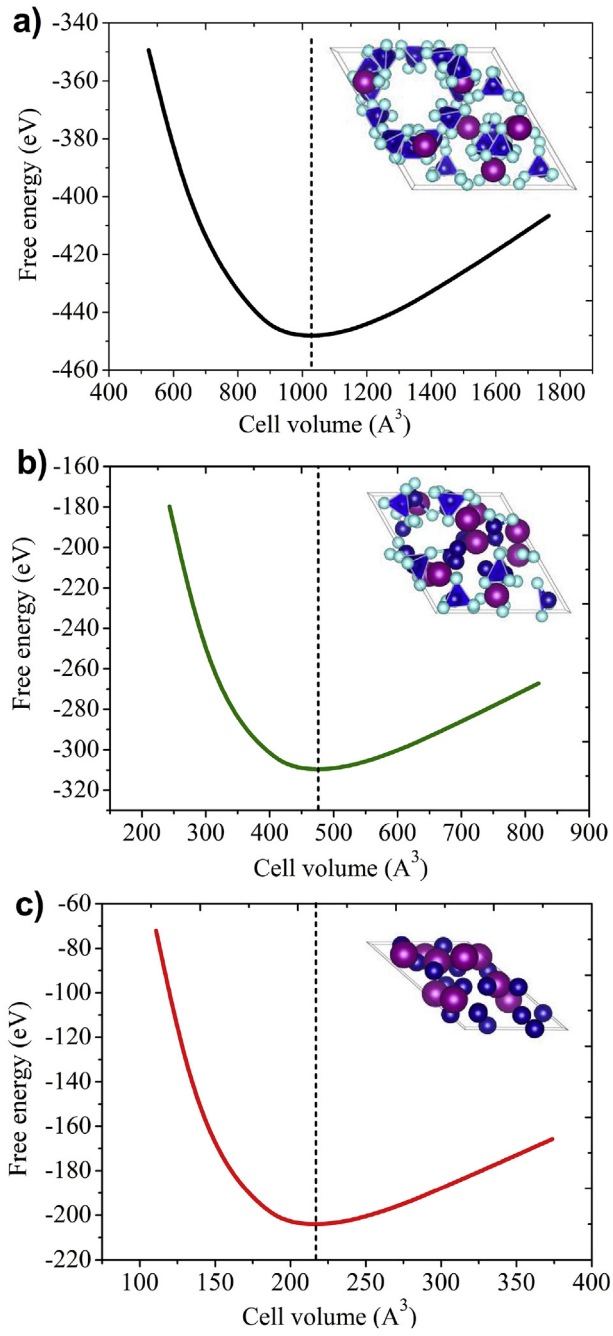

Fig. 2. Volume optimization for the initial $Mn(BH_4)_2$ unit cell (VASP#1), and hydrogen deficient unit cells of $Mn(BH_2)_2$ and $Mn(BH_0)_2$ (VASP#2 and VASP#3 correspondingly). Insets show the relaxed unit cells with Mn atoms as violet spheres, boron atoms as deep blue spheres and hydrogens - as light blue. (For interpretation of the references to colour in this figure legend, the reader is referred to the web version of this article.)

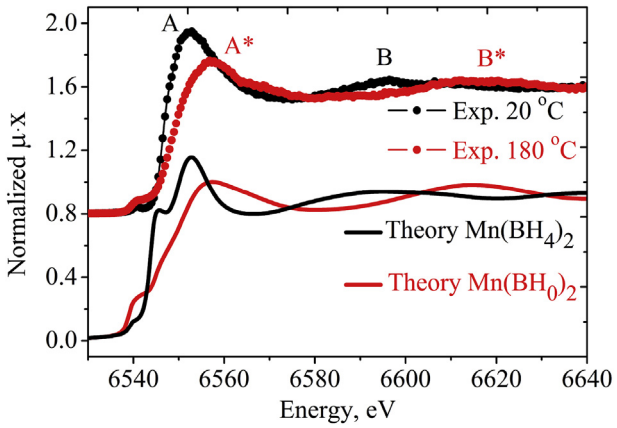

Fig. 3. Experimental (top) Mn K-edge XANES spectra for the initial and final stages of the hydrogen desorption compared to the computed ones (bottom) for the $Mn(BH_4)_2$ framework with different content of hydrogen.

case. Upper curves in Fig. 3 show changes in Mn K-edge XANES upon heating. Major changes in the peak intensities and their energy positions occur at 120 °C and no changes were observed up to the 180 °C - the highest temperature used in the experiment. Semi-empirical Natoli's rule [60,61] applied to the initial and final experimental spectra suggests the decrease of interatomic distances in the nearest coordination spheres of Mn atoms upon heating in agreement with the values reported in Table 1 for 100% and 0% of hydrogen content. Theoretical spectra presented in Fig. 3 (bottom curves) were obtained by averaging over all non-equivalent Mn atoms in the $Mn(BH_4)_2$ unit cell before and after hydrogen desorption. Calculated Mn K-edge XAS spectra for the initial (VASP#1) and collapsed $Mn(BH_4)_2$ framework without hydrogen (VASP#3) are in a good agreement with experimental data. This fact verifies the structural models obtained in DFT calculations.

Formation of Mn metallic phase as a possible decomposition product was reported in works [16,30]. Thermal analysis [29] revealed that manganese boride can exist in a number of other forms: Mn_2B, Mn_3B_4, MnB, and MnB_4. In accordance with XRPD and differential scanning calorimetry (DSC) analysis, a formation of amorphous Mn and B was shown as a result of $Mn(BH_4)_2$ thermal decomposition after 250 °C [62]. In the work of Varin et al. [51], a formation of amorphous Mn metallic phase is also suggested as a decomposition product of mechanochemically synthesized amorphous $Mn(BH_4)_2$. However, the experimental XAS spectrum for the compound after heating is different from the metallic Mn (see Fig. S3 in SI). We have performed linear combination analysis using experimental metallic Mn spectrum and theoretical spectra for $Mn(BH_0)_2$ and Mn-B systems discussed in Section 3.3 as references. Fitting results indicate that concentration of metallic Mn phase in the manganese borohydride after hydrogen desorption does not exceed 5%.

Table 1
The result of geometry optimization for Mn borohydride structure with different hydrogen content. VASP#1 is the relaxed structure of initial $Mn(BH_4)_2$ cell, VASP#2 is the relaxed structure of the cell with 50% vacant hydrogen sites and VASP#3 is a relaxed cell without hydrogen $Mn(BH_0)_2$. Both mean values and corresponding standard deviation for the nearest Mn-B and Mn-Mn distances are reported.

	Hydrogen content, %	Average Mn-B distance (Å)	Average Mn-Mn distance (Å)	Volume of the unit cell (Å^3)	Average Mn coordination number	Ref.
Exp. $Mn(BH_4)_2$	100	2.44 ± 0.02	4.80 ± 0.01	1021.8	4.00	[17]
VASP#1	100	2.41 ± 0.01	4.77 ± 0.01	1028.0	4.00	This work
VASP#2	50	2.28 ± 0.09	3.88 ± 0.24	475.8	4.66	This work
VASP#3	0	2.17 ± 0.05	2.72 ± 0.18	216.3	9.33	This work

3.3. Structure prediction of the final Mn-B phase

XANES Mn K-edge spectra for various crystalline manganese borides Mn_2B, Mn_3B_4, MnB, MnB_2 and MnB_4 as a possible candidate for the final state of the material were calculated and shown in Fig. 4c (see also Table S2 in SI for details on the boride structures, all structures were obtained from the Inorganic Crystallography Database (ICSD)). Analyzing the radial distribution functions (RDF) for the Mn local atomic structure (Fig. 4a,b) we found that shape of the XAS spectrum is rather affected by the Mn-B and Mn-Mn distances than by the stoichiometry of the compounds. Though MnB_2 and $Mn(BH_4)_2$ have the same Mn:B ratio the calculated spectrum for MnB_2 does not reproduce experimental curve for $Mn(BH_4)_2$ after heating due to the differences in Mn-B and Mn-Mn distances. In contrast, simulated spectra for Mn_2B, MnB, and MnB_4 are in a better agreement with experimental data. The interatomic Mn-B and Mn-Mn distances in these borides are in the range 2.17–2.21 Å and 2.46–2.95 Å respectively that are close to 2.17 ± 0.05 and 2.72 ± 0.18 for the relaxed $Mn(BH_0)_2$ VASP#3 structure. More details about the atomic order in these structures are evident from the RDF analysis, presented in panels 4a and 4b.

ICSD database contains two polymorphic structures for MnB_2. We show in Fig. 4 only one spectrum which fits better the experimental curve. The Mn-B and Mn-Mn distances in the crystalline MnB_2 are larger than expected in the collapsed $Mn(BH_4)_2$ framework upon hydrogen release (compare blue and gray RDF curves in Fig. 4 a,b). Therefore peak B in the theoretical spectrum for MnB_2 (blue curve in Fig. 4c) is shifted to the lower energy relative to the experimental spectrum that is in agreement with Natoli's rule [60,61].

An alternative approach to constructing the structure for the amorphous Mn-B phase is based on evolutionary algorithm search [47-49,63]. No significant sublimation process of volatile hydrogen-boron compounds was observed during heating of manganese borohydride (see TGA and mass spectroscopy data: the only negligible amount of B-containing borohydride, for example, diborane B_2H_6 were observed by Varin et al. [62]). Also, metallic Mn was excluded by means of XAS analysis described above. Therefore the Mn:B ratio was chosen according to the stoichiometry of the initial material $Mn(BH_4)_2$ i.e. 1:2. An amorphous phase could be the best candidate and thus we perform a search using extended unit cells with up to 30 atoms to simulate disorder effects.

Five structural models with the lowest value of the free energy were selected and described in Table 2 (see also Fig. S4 in SI). The density of the generated structures varies in the range 5.54 g/cm^3 - 5.79 g/cm^3. This value is larger than 5.29 g/cm^3 for relaxed $Mn(BH_0)_2$ (VASP#3 structure) obtained by removal of all hydrogen atoms from crystallographic manganese borohydride. The enthalpies per volume (density of enthalpy) calculated for all structural models are similar and vary from −0.74 to −0.80 eV/Å^3. For the experimental crystalline manganese borides, we obtained lower densities of enthalpy except for MnB_4. The enthalpy density calculated for MnB_4 was −0.84 eV/Å^3 which is significantly larger compared to other crystalline borides and models considered in this work. The enthalpy density increases along with Mn:B ratio decrease.

Table 2 shows structural parameters, densities and enthalpies per volume for structural models obtained by evolutionary algorithm search compared to the collapsed $Mn(BH_0)_2$ framework. Since several Mn and B nonequivalent positions can exist in the unit cell we report mean values for the interatomic distances and corresponding standard deviations to provide an estimation of the disorder in the local coordination of Mn. Mn-B and Mn-Mn interatomic distances for the generated structures span in the range 2.17–2.20 Å and 2.71–2.78 Å respectively. These values are close to the $Mn(BH_0)_2$ VASP#3 structure and correlate with the distances in crystalline borides Mn_2B, MnB and MnB_4. The calculated Mn K-edge XAS and radial distribution functions for structural models obtained by the evolutionary algorithm are presented in Fig. 5. Disorder in the structures is related to the broadening of the maxima in the RDF functions: single sharp peaks correspond to the ordered phase.

Numerical analysis of the discrepancy between experimental and theoretical XANES simulations shows that structures USP#2 and USP#3 are the best candidates for the decomposition reaction products. However, the enthalpies of these structures (see Table 2)

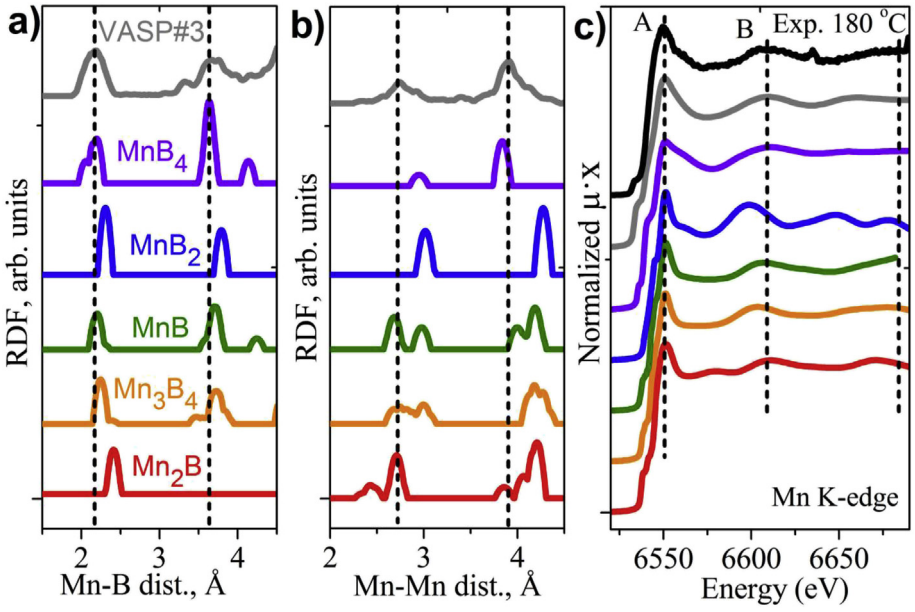

Fig. 4. Radial distribution functions for Mn-B (a) and Mn-Mn (b) distances and corresponding Mn K-edge XAS for crystalline manganese borides (c). Data for the relaxed hydrogen-free structure of $Mn(BH_0)_2$ (VASP#3) was added for comparison.

Table 2
Averaged interatomic distances, densities and enthalpies for the MnB_2 models with lowest energies obtained by the evolutionary algorithm search.

Models	Stoichiometry	Mn-B Distance (Å)	Mn-Mn Distance (Å)	Density (g/cm^3)	Hydrogen content, %	Enthalpy per volume (eV/Å^3)	Methods
VASP#3	Mn_9B_{18}	2.17 ± 0.05	2,72 ± 0.18	5.290	0	−0.7323	DFT + conjugate gradients + MD
USP#1	Mn_9B_{18}	2.19 ± 0.05	2,74 ± 0.05	5.545	0	−0.7472	DFT + evolutionary algorithm
USP#2	Mn_9B_{18}	2.18 ± 0.04	2,71 ± 0.05	5.553	0	−0.7437	DFT + evolutionary algorithm
USP#3	Mn_9B_{18}	2.20 ± 0.05	2,72 ± 0.05	5.545	0	−0.7472	DFT + evolutionary algorithm
USP#4	Mn_8B_{16}	2.18 ± 0.07	2,78 ± 0.05	5.798	0	−0.7988	DFT + evolutionary algorithm
USP#5	Mn_8B_{16}	2.17 ± 0.05	2,57 ± 0.01	5.757	0	−0.7711	DFT + evolutionary algorithm

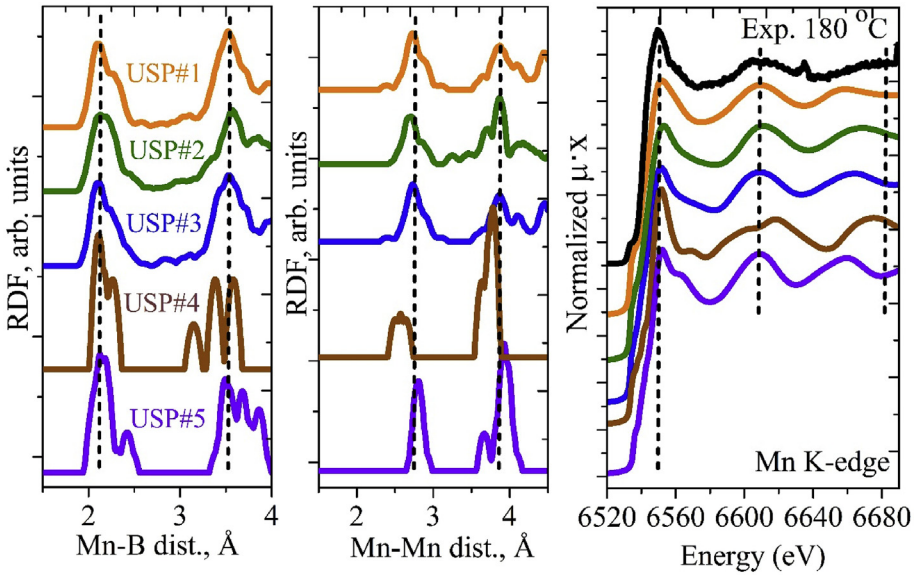

Fig. 5. Radial distribution functions for Mn-B (a) and Mn-Mn (b) distances and corresponding Mn K-edge XAS (c) for structural models predicted by means of an evolutionary algorithm.

are higher than for USP#4 and USP#5 which fit the experimental spectrum worse. We attribute this fact to the existing energy barrier for Mn-B system to be overcome before the transition in the densest structure with the lowest enthalpy. The temperature in our experiment did not exceed 200 °C and thus was too low to overcome this barrier. This is also a reason why stable crystalline phase MnB_2 failed to reproduce Mn K-edge spectrum for the $Mn(BH_4)_2$ after heating (see Fig. 4).

Other possible stoichiometries of manganese borides were also considered in evolutionary algorithm search. We calculated unit cell parameters and atomic coordinates for the MnB_4, MnB, and Mn_2B which are shown in SI. Using X-ray absorption spectroscopy as a verification tool (see Fig. S5) we can conclude that best candidates for the final amorphous manganese boride system have two maxima in Mn-B RDF functions located around 2.2 Å and 3.6 Å while peaks in Mn-Mn RDF shift along with boron fraction in the composition.

4. Conclusions

X-ray powder diffraction in conjunction with thermogravimetric analysis reveals amorphization process which is accompanied by abundant hydrogen release when the temperature of the $Mn(BH_4)_2$ exceeds 120 °C. The mass loss mainly corresponds to the release of all hydrogen atoms from the framework structure. Significant changes in the local atomic structure at the same temperature range were observed by means of X-ray absorption spectroscopy above Mn K-edge. Density functional theory calculations predict the collapse of the $Mn(BH_4)_2$ framework upon hydrogen release. Structural parameters of the amorphous collapsed phase were estimated from quantitative analysis of XAS spectra using structures generated by means of evolutionary algorithms. The predicted average Mn-B and Mn-Mn distances in manganese borides, 2.17 ± 0.05 Å and 2.72 ± 0.18 correspondingly, are in a good agreement with those predicted by Natoli's rule [60,61] applied to experimental XANES spectra. The averaged coordination number of for the first B shell around Mn for the most favorable models is estimated as 9. The radial distribution functions for the structures that fit experimental spectrum have broad peaks that evidences amorphous character of the $Mn(BH_0)_2$ down to the atomic-scale level.

Based on the experimental and computational results we propose that thermal decomposition of $Mn(BH_4)_2$ implies a formation of dense amorphous manganese borides while the concentration of Mn metallic phase is estimated below 5%.

Available spectroscopic data is less sensitive to the deviations in the Mn:B stoichiometry than to the variation of the Mn local coordination. Considering MnB_2 as the most probable reaction product we show that stable crystalline manganese diboride phase with the lowest enthalpy does not fit experimental XAS spectrum of the $Mn(BH_4)_2$ after hydrogen release. We explain this by nonequilibrium MnB_2 phase formed in the experiment which requires a certain energy barrier to be overcome before the transition to a global minimum, while the temperature in our experiment did not exceed 200 °C and thus was not high enough.

Details on crystal structure, enthalpies per volume, XRD analysis, metallic Mn K-edge XANES and Mn-Mn and Mn-B RDF for the most stable structural models predicted with stoichiometry Mn:B

equal 2:1, 1:1 and 1:4 (PDF). CIF files for the structural models discussed in the paper with stoichiometry Mn:B = 2:1, 1:1, 1:2 and 1:4 (ZIP archive).

Author contributions

The manuscript was written through contributions of all authors. All authors have given approval to the final version of the manuscript.

Funding sources

Grant of the Southern Federal University (VnGr-07/2017- 08).
Belgian Fonds National pour la Recherche Scientifique (FNRS).

Notes

The authors declare no competing financial interest.

Acknowledgment

AAG, KAL, ALB acknowledge the Grant of the Southern Federal University (VnGr-07/2017- 08) for the financial support. NAT and YF acknowledge Belgian Fonds National pour la Recherche Scientifique (FNRS CC 1.5169.12, PDR T.0169.13, EQP U.N038.13) for the financial support.

Abbreviations

DFT	density functional theory
XRD	X-ray diffraction
XRPD	X-ray powder diffraction
XAS	X-ray absorption spectroscopy
XANES	X-ray absorption near edge structure
SCF	self-consistent field
TGA	thermogravimetric analysis
RDF	Radial distribution function
SI	supplementary information

Appendix A. Supplementary data

Supplementary data related to this article can be found at https://doi.org/10.1016/j.jallcom.2017.11.062.

References

[1] H.-W. Li, Y. Yan, S.-i. Orimo, A. Züttel, C.M. Jensen, Recent progress in metal borohydrides for hydrogen storage, Energies 4 (2011) 185–214.
[2] G. Pripicini, F. Agresti, A. Maddalena, S.L. Russo, The problem of solid state hydrogen storage, Energy 34 (2009) 2087–2091.
[3] P.E. de Jongh, P. Adelhelm, Nanosizing and nanoconfinement: new strategies towards meeting hydrogen storage goals, ChemSusChem 3 (2010) 1332–1348.
[4] X. Chen, C. Li, M. Gratzel, R. Kostecki, S.S. Mao, Nanomaterials for renewable energy production and storage, Chem. Soc. Rev. 41 (2012) 7909–7937.
[5] M. Paskevicius, L.H. Jepsen, P. Schouwink, R. Cerny, D.B. Ravnsbaek, Y. Filinchuk, M. Dornheim, F. Besenbacher, T.R. Jensen, Metal borohydrides and derivatives - synthesis, structure and properties, Chem. Soc. Rev. 46 (2017) 1565–1634.
[6] V. Ban, A.V. Soloninin, A.V. Skripov, J. Hadermann, A. Abakumov, Y. Filinchuk, Pressure-collapsed amorphous $Mg(BH_4)_2$: an ultradense complex hydride showing a reversible transition to the porous framework, J. Phys. Chem. C 118 (2014) 23402–23408.
[7] A. Züttel, Materials for hydrogen storage, Mater. Today 6 (2003) 24–33.
[8] A. Züttel, P. Wenger, S. Rentsch, P. Sudan, P. Mauron, C. Emmenegger, $LiBH_4$ a new hydrogen storage material, J. Power Sources 118 (2003) 1–7.
[9] J-Ph Soulie, G. Renaudin, R. Cerny, K. Yvon, Lithium boro-hydride $LiBH_4$, J. Alloys Compd. 346 (2002) 200–205.
[10] Z. Łodziana, T. Vegge, Structural stability of complex hydrides: $LiBH_4$, Phys. Rev. Lett. 93 (2004) 145501.
[11] J.J. Vajo, S.L. Skeith, F. Mertens, Reversible storage of hydrogen in destabilized $LiBH_4$, J. Phys. Chem. B 109 (2005) 3719–3722.
[12] A. Zuttel, S. Rentsch, P. Fischer, P. Wenger, P. Sudan, Ph. Mauron, C. Emmenegger, Hydrogen storage properties of $LiBH_4$, J. Alloys Compd. 356-357 (2003) 515–520.
[13] C. Li, P. Peng, D.W. Zhou, L. Wan, Research progress in $LiBH_4$ for hydrogen storage: a review, Int. J. Hydrog. Energy 36 (2011) 14512–14526.
[14] K. Miwa, N. Ohba, S.-i. Towata, Y. Nakamori, S.-i. Orimo, First-principles study on lithium borohydride $LiBH_4$, Phys. Rev. B 69 (2004) 245120.
[15] Y. Yan, A. Remhof, D. Rentsch, A. Zuttel, The role of $MgB_{12}H_{12}$ in the hydrogen desorption process of $Mg(BH_4)_2$, Chem. Commun. 51 (2015) 700–702.
[16] Pabitra Choudhury, Venkat R. Bhethanabotla, E. Stefanakos, Manganese borohydride as a hydrogen-storage candidate: first-principles crystal structure and thermodynamic properties, J. Phys. Chem. C 113 (2009) 13416–13424.
[17] R. Cerny, N. Penin, H. Hagemann, Y. Filinchuk, The first crystallographic and spectroscopic characterization of a 3d-metal borohydride: $Mn(BH_4)_2$, J. Phys. Chem. C (2009) 9003–9007.
[18] N.A. Tumanov, D.A. Safin, B. Richter, Z. Łodziana, T.R. Jensen, Y. Garcia, Y. Filinchuk, Challenges in the synthetic routes to $Mn(BH_4)_2$: insight into intermediate compounds, Dalton Trans. 44 (2015) 6571–6580.
[19] B. Richter, D.B. Ravnsbæk, N. Tumanov, Y. Filinchuk, T.R. Jensen, Manganese borohydride; synthesis and characterization, Dalton Trans. 44 (2015) 3988–3996.
[20] Y. Filinchuk, B. Richter, T.R. Jensen, V. Dmitriev, D. Chernyshov, H. Hagemann, Porous and dense magnesium borohydride frameworks: synthesis, stability, and reversible absorption of guest species, Angew. Chem. Int. Ed. 50 (2011) 11162–11166.
[21] N.A. Tumanov, E. Roedern, Z. Łodziana, D.B. Nielsen, T.R. Jensen, A.V. Talyzin, R. Černý, D. Chernyshov, V. Dmitriev, T. Palasyuk, Y. Filinchuk, High-pressure study of $Mn(BH_4)_2$ reveals a stable polymorph with high hydrogen density, Chem. Mater. 28 (2016) 274–283.
[22] G.N. Kalantzopoulos, J.G. Vitillo, E. Albanese, E. Pinatel, B. Civalleri, S. Deledda, S. Bordiga, M. Baricco, B.C. Hauback, Hydrogen storage of Mg-Zn mixed metal borohydrides, J. Alloys Compd. 615 (2014) 702–705.
[23] R. Bonaccorsi, O. Charkin, J. Tomasi, Nonempirical study of the structure and stability of beryllium, magnesium, and calcium borohydrides, Inorg. Chem. 30 (1991) 2964–2969.
[24] L. George, S.K. Saxena, Structural stability of metal hydrides, alanates and borohydrides of alkali and alkali- earth elements: a review, Int. J. Hydrog. Energy 35 (2010) 5454–5470.
[25] Y. Nakamori, K. Miwa, A. Ninomiya, H. Li, N. Ohba, S.-i. Towata, A. Züttel, S.-i. Orimo, Correlation between thermodynamical stabilities of metal borohydrides and cation electronegativites: first-principles calculations and experiments, Phys. Rev. B 74 (2006) 045126.
[26] E. Roedern, Y.-S. Lee, M.B. Ley, K. Park, Y.W. Cho, J. Skibsted, T.R. Jensen, Solid state synthesis, structural characterization and ionic conductivity of bimetallic alkali-metal yttrium borohydrides $M(BH_4)_4$ (M = Li and Na), J. Mater. Chem. A 4 (2016) 8793–8802.
[27] K. Miwa, M. Aoki, T. Noritake, N. Ohba, Y. Nakamori, S.-i. Towata, A. Züttel, S.-i. Orimo, Thermodynamical stability of calcium borohydride $Ca(BH_4)_2$, Phys. Rev. B 74 (2006).
[28] J.G. Vitillo, S. Bordiga, M. Baricco, Spectroscopic and structural characterization of thermal decomposition of γ-$Mg(BH_4)_2$: dynamic vacuum versus H_2 atmosphere, J. Phys. Chem. C 119 (2015) 25340–25351.
[29] W. Sun, Y. Du, S. Liu, B. Huang, C. Jiang, Thermodynamic assessment of the Mn-B system, J. Phase Equilib. Diffus. 31 (2010) 357–364.
[30] R. Liu, D. Reed, D. Book, Decomposition behaviour of $Mn(BH_4)_2$ formed by ball-milling $LiBH_4$ and $MnCl_2$, J. Alloys Compd. 515 (2012) 32–38.
[31] P.M. Abdala, O.V. Safonova, G. Wiker, W. van Beek, H. Emerich, J. van Bokhoven, J.A. Sa, J. Szlachetko, M. Nachtegaal, Scientific opportunities for heterogeneous catalysis research at the SuperXAS and SNBL beam lines, Chimia 66 (2012) 699–705.
[32] W. Van Beek, O.V. Safonova, G. Wiker, H. Emerich, SNBL, a dedicated beamline for combined in situ X-ray diffraction, X-ray absorption and Raman scattering experiments. Phase Transit. 84 (2011) 726–732.
[33] A.L. Bugaev, A.A. Guda, K.A. Lomachenko, V.V. Shapovalov, A. Lazzarini, J.G. Vitillo, L.A. Bugaev, E. Groppo, R. Pellegrini, A.V. Soldatov, J.A. Van Bokhoven, C. Lamberti, Core-shell structure of palladium hydride nanoparticles revealed by combined x-ray absorption spectroscopy and x-ray diffraction, J. Phys. Chem. C 121 (2017) 18202–18213.
[34] C.W. Andersen, E. Borfecchia, M. Bremholm, M.R.V. Jørgensen, P.N.R. Vennestrøm, C. Lamberti, L.F. Lundegaard, B.B. Iversen, Redox-driven migration of copper ions in the Cu-CHA zeolite as shown by the in situ PXRD/XANES technique, Angew. Chem. Int. Ed. 56 (2017) 10367–10372.
[35] B. Ravel, M. Newville, ATHENA, ARTEMIS, HEPHAESTUS: data analysis for X-ray absorption spectroscopy using IFEFFIT, J. Synchrotron Radiat. 12 (2005) 537–541.
[36] A.P. Hammersley, S.O. Svensson, M. Hanfland, A.N. Fitch, D. Hausermann, Two-dimensional detector software: from real detector to idealised image or two-theta scan, High Press. Res. 14 (1996) 235–248.
[37] T.A. Davis, Algorithm 832: UMFPACK V4.3 an unsymmetric-pattern multifrontal method, ACM Trans. Math. Software 30 (2004) 196–199.
[38] Y. Joly, X-ray absorption near-edge structure calculations beyond the muffin-tin approximation, Phys. Rev. B 63 (2001) 125120.

[39] Y. Joly, S. Grenier, Theory of X-ray absorption near edge structure, in: J.A. van Bokhoven, C. Lamberi (Eds.), X-Ray Absorption and X-Ray Emission Spectroscopy, John Wiley & Sons, Chichester (UK), 2016, pp. 73–97.
[40] S.A. Guda, A.A. Guda, M.A. Soldatov, K.A. Lomachenko, A.L. Bugaev, C. Lamberti, W. Gawelda, C. Bressler, G. Smolentsev, A.V. Soldatov, Y. Joly, Optimized finite difference method for the full-potential XANES simulations: application to molecular adsorption geometries in MOFs and metal-ligand intersystem crossing transients, J. Chem. Theory Comput. 11 (2015) 4512–4521.
[41] A.A. Guda, S.A. Guda, M.A. Soldatov, K.A. Lomachenko, A.L. Bugaev, C. Lamberti, W. Gawelda, C. Bressler, G. Smolentsev, A.V. Soldatov, Y. Joly, Finite difference method accelerated with sparse solvers for structural analysis of the metal-organic complexes, J. Phys. Conf. Ser. 712 (2016) 12004.
[42] G. Kresse, J. Furthmüller, Efficiency of ab-initio total energy calculations for metals and semiconductors using a plane-wave basis set, Comput. Mater. Sci. 6 (1996) 15–50.
[43] G. Kresse, J. Furthmüller, Efficient iterative schemes for ab initio total-energy calculations using a plane-wave basis set, Phys. Rev. B 54 (1996) 11169–11186.
[44] G. Kresse, D. Joubert, From ultrasoft pseudopotentials to the projector augmented-wave method, Phys. Rev. B 59 (1999) 1758–1775.
[45] W.H. Press, B.P. Flannery, S.A. Teukolsky, W.T. Vetterling, Numerical Species, Cambridge University press, New York, 1986.
[46] H.J. Monkhorst, J.D. Pack, Special points for Brillouin-zone integrations, Phys. Rev. B 13 (1976) 5188–5192.
[47] C.W. Glass, A.R. Oganov, N. Hansen, USPEX - evolutionary crystal structure prediction, Comput. Phys. Commun. 175 (2006) 713–720.
[48] A.R. Oganov, C.W. Glass, Crystal structure prediction using ab initio evolutionary techniques: principles and applications, J. Chem. Phys. 124 (2006) 244704.
[49] A.R. Oganov, A.O. Lyakhov, M. Valle, How evolutionary crystal structure prediction works - and why, Acc. Chem. Res. 44 (2011) 227–236.
[50] A.A. Guda, I.A. Pankin, A.L. Bugaev, K.A. Lomachenko, S.A. Guda, V.P. Dmitriev, A.V. Soldatov, X-ray absorption spectroscopy determination of the products of manganese borohydride decomposition upon heating, Bull. Russ. Acad. Sci. Phys. 79 (2015) 139–143.
[51] R.A. Varin, D.K. Mattar, A.S. Bidabadi, M. Polanski, Synthesis of amorphous manganese borohydride in the ($NaBH_4$–$MnCl_2$) system, its hydrogen generation properties and crystalline transformation during solvent extraction, J. Energy Chem. 26 (2017) 24–34.
[52] G. Severa, H. Hagemann, M. Longhini, J.W. Kaminski, T.A. Wesolowski, C.M. Jensen, Thermal desorption, vibrational spectroscopic, and DFT computational studies of the complex manganese borohydrides $Mn(BH_4)_2$ and $[Mn(BH_4)_4]^{2-}$, J. Phys. Chem. 114 (2010) 15516–15521.
[53] J.J. Rehr, R.C. Albers, Theoretical approaches to x-ray absorption fine structure, Rev. Mod. Phys. 72 (2000) 621–654.
[54] J.J. Rehr, A.L. Ankudinov, Progress in the theory and interpretation of XANES, Coord. Chem. Rev. 249 (2005) 131–140.
[55] S. Bordiga, E. Groppo, G. Agostini, J.A. van Bokhoven, C. Lamberti, Reactivity of surface species in heterogeneous catalysts probed by in situ x-ray absorption techniques, Chem. Rev. 113 (2013), 1736–1850.
[56] J. Van Bokhoven, C. Lamberti, in: X-Ray Absorption and X-ray Emission Spectroscopy: Theory and Applications, John Wiley & Sons, Chichester (UK), 2016.
[57] G.N. Greaves, EXAFS and the structure of glass, J. Non-Cryst. Solids 71 (1985) 203–217.
[58] A. Filipponi, A. Di Cicco, Short-range order in crystalline, amorphous, liquid, and supercooled germanium probed by x-ray-absorption spectroscopy, Phys. Rev. B 51 (1995) 12322–12336.
[59] A. Filipponi, EXAFS for liquids, J. Phys. Condens. Matter. 13 (2001) R23–R60.
[60] A. Bianconi, M. Dell Ariccia, A. Gargano, C.R. Natoli, in: A. Bianconi, L. Incoccia, S. Stipcich (Eds.), EXAFS and Near Edge Structure I, Springer Series in Chemical Physics, 27, 1983, pp. 57–61. Berlin.
[61] C.R. Natoli, in: K.O. Hodgson, B. Hedman, J.E. Penner-Hahn (Eds.), EXAFS and Near Edge Structure III, Springer Series in Chemical Physics, 2, 1984, pp. 38–42. Berlin.
[62] R.A. Varin, A.S. Bidabadi, The effect of milling energy input during mechanochemical activation synthesis (MCAS) of the nanocrystalline manganese borohydride $Mn(BH_4)_2$ on its thermal dehydrogenation properties, Int. J. Hydrog. Energy 39 (2014) 11620–11632.
[63] A.O. Lyakhov, A.R. Oganov, M. Valle, How to predict very large and complex crystal structures, Comput. Phys. Commun. 181 (2010) 1623–1632.